Check for updates

Enhancing light harvesting in bilayered dye-sensitized solar cells by tailoring light scattering with electrospun TiO₂ nanofibers†

Manikandan M., [iD] [ab] Anooja J., [ab] Narayanan Unni K. N., [iD] [ab] Suraj Soman [iD] *[ab] and Sujatha Devi P. [iD] *[ab]

Dye-sensitised solar cells (DSCs) possess promising features such as high performance under low-light conditions, cost-effectiveness, and adaptability in contrast to conventional silicon-based solar cells. Introducing a scattering layer has been reported to be one of the most effective and economical solutions for improving the efficiency of DSCs. In this regard, various one-dimensional nanostructures have been applied to DSCs to enhance its light scattering property and improve electron transport, thereby achieving a better lifetime. This study highlights the potential advantages of using the well-known electrospinning technique to synthesize various phases of TiO₂ fibers that are effective scattering layers for achieving enhanced light harvesting through improved light scattering and dye anchoring. It was observed that the scattering layer consisting of anatase phase TiO₂ fibers enhanced the power conversion efficiency of nanoparticle-based devices by 60% (8.67% ± 0.58%) primarily owing to the combined effects of improved light harvesting through light scattering and enhanced dye anchoring. However, the rutile phase TiO₂ fibers, as a scattering layer, increased the power conversion efficiency only by 45% (7.85% ± 0.47%). Additionally, perturbation techniques used to investigate the impact of the TiO₂ fiber scattering layer on electron transfer dynamics revealed that the TiO₂ fiber layer contributed to a long electron lifetime and facilitated rapid electron diffusion, thereby promoting efficient charge collection.

I. Introduction

In the past few decades, dye-sensitized solar cells (DSCs) have gained popularity as a photovoltaic technology owing to their cost-effectiveness, ease of fabrication, and ability to modify their structures. A reasonably high power conversion efficiency (PCE) of 15.2% under one sun irradiation has been demonstrated by DSCs.[1,2] Recently, DSCs have been further improved to perform under indoor light conditions, with their efficiency reaching up to 40%.[3–6] Photoanode, dye, electrolyte, and counter electrode are the four primary components of a conventional DSC, each of which has been investigated by various researchers for improving device performances.[7–11]

Among the different strategies and modifications employed to improve the overall efficiency of DSCs, the addition of a scattering layer over the active layer has proven to be an efficient way to enhance the device performance.[12–15] Adding

a scattering layer provides long paths for lights and thus improves the light harvesting of such devices.[12] Anatase nanoparticles of different shapes and sizes are applied on DSCs as photoanodes and scattering layers.[16–19] Compared to nanoparticles, one-dimensional TiO₂ structures provide efficient scattering and direct pathways for electron transport owing to their stretched grown structure to a specific direction and reduced grain boundaries.[20,21] Electrospinning is a captivating technique for synthesizing nano-/micro-structured continuous fibers of metals, oxides, and polymers.[22] Several groups have used the electrospinning technique to synthesize TiO₂ nanofibers, nanorods, and nanotubes for DSC applications.[23,24] Joshi *et al.* reported that when compared to TiO₂ nanoparticles, electrospun TiO₂ fibers of 300 nm diameter could effectively act as scattering centres without reducing the dye loading.[20] The power conversion efficiency of the DSC fabricated with 85% nanoparticles and 15% nanofibers was 44% greater than that of the DSC fabricated exclusively with TiO₂ nanoparticles. Wang *et al.* reported transient photocurrent and photovoltage studies on nanoparticle-nanofiber composite DSCs.[25] The addition of TiO₂ nanofibers substantially improved the charge collection efficiency of photoanode owing to highly crystalline grains and fewer grain boundaries in TiO₂ nanofibers. A bilayered photoanode structure with TiO₂ nanoparticle underlayer and

Centre for Sustainable Energy Technologies (C-SET), CSIR-National Institute for Interdisciplinary Science and Technology (NIIST), Thiruvananthapuram, 695019, India. E-mail: psujathadeviniist@gmail.com; suraj@niist.res.in

Academy of Scientific and Innovative Research (AcSIR), Ghaziabad 201002, India

nanofiber scattering layer (NPs/NFs) with component roles for each layer were reported by Du et al.[26] Compared to pure TiO_2 NP-based devices, this bilayer-structured device exhibited an approximately 14% improvement in power conversion efficiency. Wang et al. improved the short-circuit current density and PCE of NP-based devices by applying an NF layer over the NP layer.[27] This NP/NF bilayered DSC achieved 8.03% PCE, which was 26% greater than that of the NP/NP photoanode devices.

All the above studies pertain to anatase TiO_2 as a scattering layer. TiO_2 particles with a large size and good crystalline nature with a rutile phase are expected to be better candidates for scattering layer applications. It is anticipated that the rutile phase of TiO_2, having a higher refractive index of 2.78 @ 500 nm than the anatase phase (2.60 @ 500 nm), although not well explored in DSC as a scattering layer, can perform as a better scattering layer than anatase.[28] For this purpose, we synthesised anatase, rutile, and anatase–rutile mixed TiO_2 fibers by electrospinning to explore their potential as photoanodes and scattering layers in DSC. Electrospinning synthesis of oxide fibers combines sol–gel chemistry with controlled combustion, and the solution composition and combustion conditions can affect the physical and chemical attributes of the resultant fibers.[29] In this context, we demonstrate the precise phase control of TiO_2 fibers through electrospinning by diligently controlling the sol composition and calcination temperatures. The synthesized fibers are characterized using the following commonly used analytical techniques: X-ray diffraction, confocal Raman spectroscopy, scanning electron microscopy, transmission electron microscopy, Brunauer–Emmett–Teller analysis, and UV-Vis absorption spectroscopy. The effect of anatase and rutile phases of TiO_2 fibers on the DSC performance was studied by applying them as the photoanode and scattering layers. In this study, in addition to regular device measurements, electrochemical impedance spectroscopy (EIS), transient photovoltage decay, and transient photocurrent decay measurements were employed to study the effect of the TiO_2 fiber scattering layer on electron transfer dynamics.

II. Experimental procedure

A. Electrospun synthesis of TiO_2 fibers

TiO_2 fibers were fabricated by electrospinning a titania sol prepared by applying a modified sol–gel technique.[30] For anatase TiO_2, the sol was made by adding 0.68 mL of acetylacetone to 10 mL of 5 wt% of polyvinylpyrrolidone (PVP, M_w = 136 000 mol g^{-1}) in ethanol, followed by the addition of 4 mL of titanium(IV) isopropoxide (TTIP).[30] After 15 minutes of stirring, 0.3 mL of deionised water was added dropwise. The mixed solution thus prepared was stirred overnight under ambient conditions to make it homogeneous. To make fibers using electrospinning, the as-prepared sol was loaded in a plastic syringe and placed horizontally in the electrospinning instrument. The solution was injected at a rate of 2 mL h^{-1} using a syringe pump, and an electric potential of 14 kV was applied at the needle tip using a high-voltage power supply. The fibers were collected on a rotating drum (450 rpm) and calcined at 500 °C for 2 hours to

remove the PVP polymer and convert TTIP into anatase TiO_2. To produce rutile and anatase–rutile mixture TiO_2 fibers, the titania sol was made in 10 mL of 30 wt% of polyvinylpyrrolidone (PVP, M_w = 55 000 mol g^{-1}) by the addition of 0.68 mL of acetylacetone (99.5%), 4 mL of TTIP, (97%) and 0.3 mL of water. For electrospinning, a flow rate of 2 mL h^{-1}, a needle-to-drum distance of 14 cm and an applied potential of 14 kV were fixed. Anatase–rutile mixture fibers were formed by calcining the fiber at 500 °C, while the rutile TiO_2 fibers were obtained at 700 °C calcination of the as-prepared fibers.

B. TiO_2 fiber paste preparation

TiO_2 fiber pastes were prepared following the commonly used paste preparation procedure in our laboratory.[31] To obtain a paste suitable for the doctor blade coating, 0.25 g of ethyl cellulose and 2.03 g of terpineol were dissolved in 5 mL of ethanol, followed by adding 0.5 g of TiO_2 fibers. The mixture was sonicated using an ultrasonic probe-sonicator for 15 minutes to mix the components homogeneously. The ethanol content was removed by keeping the paste on a hot plate at 60 °C for 30 min to make the paste viscous enough to coat on FTO glass.[31]

C. Dye loading study of films

The amount of dye adsorbed onto the fiber films was quantified through dye adsorption–desorption experiments at a temperature of 25 °C. The fiber films were immersed in a 0.5 mM N719 solution for 24 hours. Subsequently, the adsorbed dye molecules were desorbed into a 0.1 M NaOH solution in water. The number of dye molecules desorbed from each film was determined quantitatively from the absorbance of the solution.[32]

D. DSC device fabrication

Dye-sensitized solar cells were fabricated by following the previously reported protocol from our group.[33] In a typical procedure, a thin TiO_2 blocking layer was deposited on a cleaned 1.6×1.6 cm^2 FTO (TEC 10, Sigma-Aldrich) by soaking the FTO in a 40 mM TiCl$_4$ solution for 30 min at 70 °C, followed by annealing at 500 °C for 30 min. The nanoparticles (Dyesol 18NR-T) or fiber TiO_2 film (~13–14 μm thickness) were deposited on the pre-deposited FTO glass substrates using the doctor blade method. After coating the first layer, the substrate was dried at 100 °C for 10 minutes. The same doctor blade method was used to coat the second layer (~6–7 μm thickness) over the first layer and finally annealed at 500 °C for 30 min. A post-blocking layer was also deposited on the TiO_2 films as the same procedure mentioned earlier. The TiO_2 films were sensitized with N719 dye by soaking in a solution of 0.5 mM N719 and 10 mM CDCA in a 1 : 1 acetonitrile and tertiary butanol mixture for 24 hours. The counter electrode was prepared by coating Pt paste (Dyesol PT-1) on a cleaned FTO glass. The Pt paste-coated glass plates were annealed for 30 minutes at 420 °C. The electrodes were assembled in a sandwich type using UV epoxy lines as the spacer to form a solar cell. The iodide/triiodide (Greatcell Solar EL-HPE) electrolyte was filled

through the pre-drilled holes and sealed with parafilm and cover glass.

E. Material characterization

X-ray diffraction (XRD) analysis and Raman spectroscopy were used to confirm the crystallinity and phase purity of the synthesized TiO$_2$ fibers. The XRD patterns were recorded using a Malvern PANalytical X'Pert Pro MPD XRD instrument operated with Cu Kα radiation of an X-ray wavelength (λ) of 1.5406 Å. The Raman spectra were obtained using a confocal Raman instrument (Witek, Germany) equipped with a 633 nm wavelength laser in the spectral range of 100–900 cm^{-1}. Thermogravimetric analyses (TGA) and differential scanning calorimetry (DSC) measurements were performed using the PerkinElmer STA 8000 instrument over a temperature range of 40–600 °C at a heating rate of 10 °C min^{-1}. The surface morphology of the fibers was confirmed under a Carl Zeiss, Germany scanning electron microscope (SEM). To confirm the morphology of the synthesised materials, TEM analysis was carried out using a JEOL (JEM F 200 with EDS, STEM, EELS) high-resolution transmission electron microscope (HRTEM) operated at an accelerating voltage of 200 kV. The BET surface area of the samples was determined using a Tristar II Micromeritics surface area analyzer after the samples were degassed at 200 °C for 2 hours. Diffuse reflectance spectra (DRS) and transmittance of the photoanode films and UV-Vis absorption spectra of the dye solutions were recorded using a PerkinElmer Lambda 950 UV-Vis-NIR spectrometer with interchangeable snap-in modules for the solid and liquid samples.

F. Solar cell characterization

The photovoltaic characteristics of solar cells were evaluated under one sun condition (100 mW cm^{-2}, AM 1.5 G) using a Keithley source meter and a Newport class AAA solar simulator. A circular black mask of area 0.1133 cm^2 was used for the J–V measurements to avoid the impact of light falling outside the active area. The incident photon-to-current conversion efficiency (IPCE) of the devices was measured under DC mode using a 300 W xenon lamp that was integrated with a Newport monochromator and a power meter. Transient photovoltage decay and transient photocurrent decay measurements were performed using the Dyenamo Toolbox set-up (DN-AE01). Electrochemical impedance spectroscopy (EIS) measurements were carried out using an electrochemical workstation, Autolab-PGSTAT 302N (Metrohm).

III. Results and discussion

Fig. 1a shows a schematic illustration of the synthesis of TiO$_2$ fibers using the electrospinning technique. Electrospinning of TiO$_2$ sol produces a fiber mat of PVP–TTIP composite, which is then calcined in air to remove the PVP template and produce TiO$_2$ from the TTIP. The composite fibers were calcined at 500 °C, during which two key processes occurred: (1) the decomposition and burning of PVP and (2) the conversion of TTIP into TiO$_2$.

The crystal structure of the calcined fibers was characterized by X-ray diffraction (XRD) analysis. The XRD patterns of the TiO$_2$ fibers synthesised with PVP of $M_w = 136\,000$ mol g^{-1} matches well with the JCPDS card no. 01-084-1286 of the TiO$_2$ anatase phase after calcination at 500 °C. All the diffraction peaks are indexed to the reflection planes (101), (004), (200), (105), (211), (204), (220) and (125) of anatase TiO$_2$, as shown in Fig. 1b. When the fibers of the PVP of $M_w = 55\,000$ mol g^{-1} were calcined at 500 °C, the anatase–rutile mixture phase was formed. Along with anatase phase, Rutile reflection planes (110), (101), and (111) were observed, respectively, at 27.50°, 35.95°, and 41.29°. When the latter fibers were calcined at 700 °C, XRD patterns of the produced fibers matched well with the JCPDS card no. 01-072-1148 of the TiO$_2$ rutile phase, with the peaks at 27.43°, 36.12°, 41.15°, 43.98°, 54.39°, 56.63°, 62.81°, 64.12°, and 69.11° are, respectively, indexed to (110), (101), (111), (210), (211), (220), (002), (310), and (301) reflection planes of rutile TiO$_2$. From the analysis of XRD patterns, TiO$_2$ fibers of different crystal phases were synthesized by varying the polymer concentration and controlling the calcination temperature. Owing to the lower calcination temperature, the resulting TiO$_2$ fibers were in the anatase phase. However, when the calcination temperature was increased, the anatase-to-rutile phase transition occurs, resulting in rutile phase formation. The anatase TiO$_2$, anatase–rutile mixture TiO$_2$ and rutile TiO$_2$ samples are denoted as TiO$_2$-A, TiO$_2$-AR and TiO$_2$-R, respectively, in further discussions in this study. It is also observed that sample crystallinity increased with calcination temperature.[34] The fraction of the rutile phase in the mixture phase TiO$_2$-AR fiber was calculated using eqn (1) and found to be about 29%, where I_A is the integral intensity of the anatase TiO$_2$ (101) diffraction peak and I_R is the integral intensity of the rutile TiO$_2$ (110) diffraction peak.[35] The lattice parameters of the calcined samples were derived as $a = 3.7904$ Å and $c = 9.4747$ Å for TiO$_2$-A, $a = 4.1298$ Å and $c = 8.8764$ Å for TiO$_2$-AR and $a = 4.5860$ Å and $c = 2.8844$ Å for TiO$_2$-R, and all the three samples have $\alpha = \beta = \gamma = 90°$. The average crystallite sizes calculated from the Scherrer formula (eqn (2)) were 13.80 nm, 25.82 nm, and 56.26 nm for TiO$_2$-A, TiO$_2$-AR, and TiO$_2$-R, respectively.

Fraction of rutile TiO$_2$,

$$W_R = \frac{I_R}{0.8861 I_A + I_R},\qquad(1)$$

Average crystallite size,

$$D = \frac{k\lambda}{\beta \cos\theta}.\qquad(2)$$

The information derived from the Raman spectroscopic technique further corroborates the structural confirmation from the XRD analysis. Distinct peaks observed at 145, 404, 526, and 636 cm^{-1} for TiO$_2$-A (Fig. S1†) are attributed to the anatase TiO$_2$ Raman active modes E_g, B_{1g}, A_{1g}, and E_g, respectively.[36] The TiO$_2$-R exhibits rutile characteristic signals of symmetries B_{1g}, E_g, and A_{1g} at 145, 441, and 610 cm^{-1}, respectively, with the broad signal observed at 249 cm^{-1} corresponding to rutile
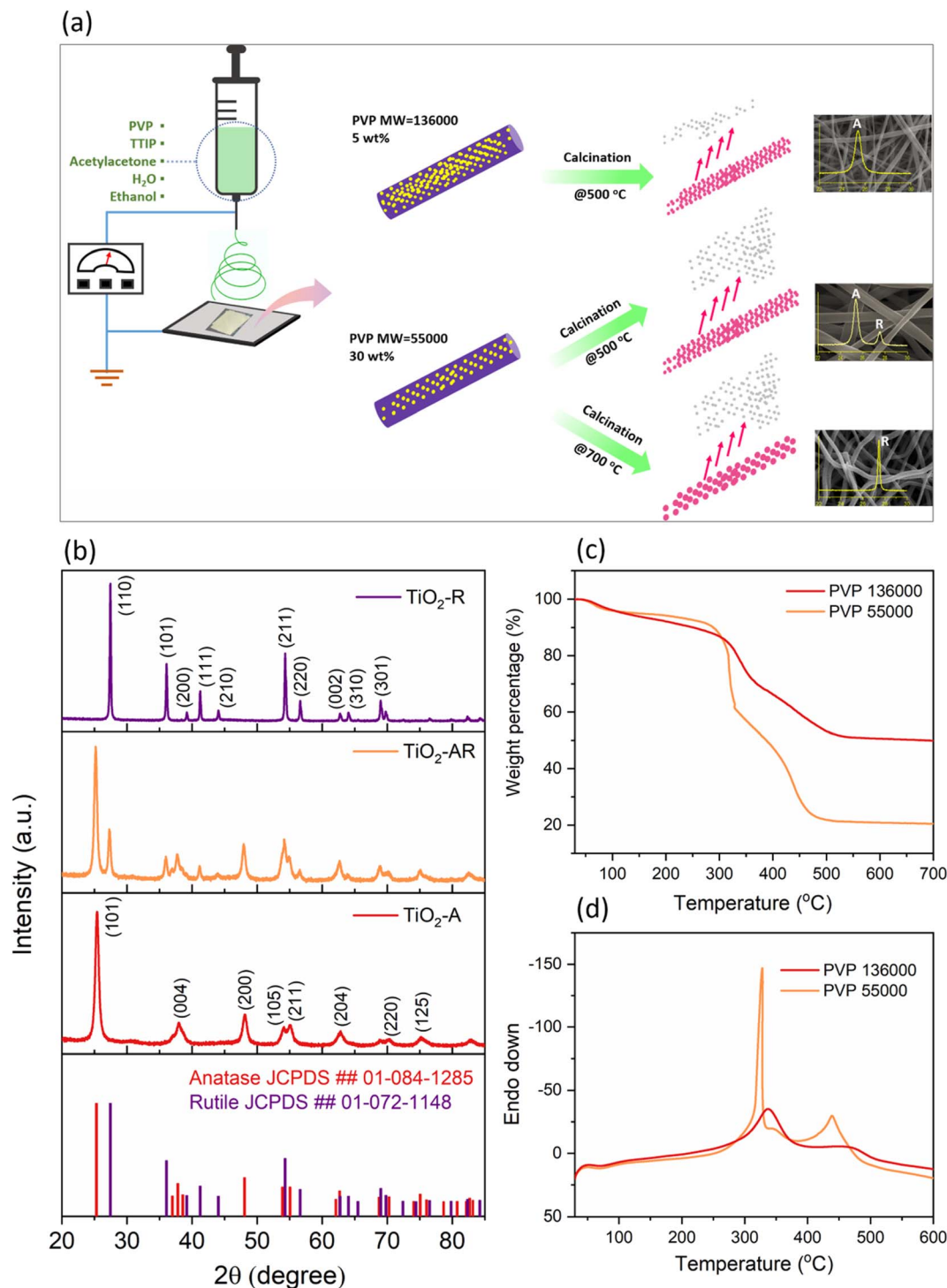
Fig. 1 (a) Schematic of the synthesis of TiO_2 fibers using the electrospinning technique. (b) XRD pattern of TiO_2 fibers after calcination along with JCPDS of anatase and rutile TiO_2. (c) TGA and (d) DSC of as-spun fibers of PVP of M_w = 55 000 mol g^{-1} and PVP of M_w = 136 000 mol g^{-1}.

phase multiple phonon scattering.[36] Conversely, TiO_2-AR reveals the presence of anatase and rutile phases, indicating the coexistence of both phases. The XRD and Raman analyses confirm the formation of TiO_2 using the electrospinning technique, with the phase being controlled by changing the sol composition and calcination temperature.

It has been demonstrated that by carefully adjusting the molecular weight and concentration of PVP, one can obtain either anatase alone or mixed anatase–rutile TiO_2 fibers when calcined at 500 °C. In the electrospinning process with PVP-based sol compositions, the PVP polymer serves a twofold purpose. Its primary function is to enhance the viscosity of the

solution for fiber formation through electrospinning.[37] The polymer concentrations in the solution are fine-tuned to be 30 and 5 weight percentages, respectively, for PVP of M_w of 55 000 mol g^{-1} and 136 000 mol g^{-1}. This precise composition results in bead-free continuous PVP–TTIP composite fibers. A higher weight percentage of lower molecular weight PVP (M_w = 55 000 mol g^{-1}) was necessary owing to its reduced efficiency in elevating the solution viscosity. In contrast, a lower concentration suffices for the higher molecular weight PVP (M_w = 136 000 mol g^{-1}) to attain the desired viscosity. Then, the polymer functions as a sacrificial template and imparts the fibrous structure to TiO$_2$ during the calcination of the as-spun PVP–TTIP composites.[30]

The effects of polymer molecular weight and weight percentage on decomposition and crystallisation were investigated using TGA-DSC analysis. The crystallisation of TiO$_2$ occurs during the calcination steps.[38] The thermograms of the composite fibers are illustrated in Fig. 1c, capturing the distinct thermal behaviours. Attributable to the differences in weight percentages, the PVP (M_w = 55 000 mol g^{-1})–TTIP composite exhibited a higher weight loss than the PVP (M_w = 136 000 mol g^{-1})–TTIP composite. Despite the weight loss, both thermograms share a comparable decomposition profile. The initial weight loss in the range of 50–100 °C is ascribed to the solvent volatilisation. The pronounced weight loss observed in the 300–310 °C range can be linked to the thermal decomposition of the PVP polymer molecules and the organic parts of the TTIP.[39] Notably, the decomposition curve of the higher molecular weight PVP (M_w = 136 000 mol g^{-1}) fibers exhibited a gentle decline owing to the higher degree of polymerisation.[40] Subsequent to this second weight loss, a third weight loss was observed for both samples. Because of the fast decomposition of the lower molecular weight polymer, the third weight loss of PVP of M_w = 55 000 mol g^{-1} fibers occurs more readily at 310 °C. Meanwhile, the fibers of PVP of M_w = 136 000 mol g^{-1} decompose slowly, and the third weight loss occurs at 350 °C. This final weight loss is attributed to the combustion of carbon residues formed from the decomposed PVP.[39] Significantly, no weight loss occurs after 500 °C, affirming the efficiency of calcination of the fibres at 500 °C to produce TiO$_2$ fibres from the PVP–TTIP composite by removing all other organic and solvent residues.

Crystallisation necessitates heat energy to migrate atoms into lattice positions that are thermodynamically disfavoured at lower temperatures.[41] DSC is a valuable tool for evaluating the change in heat flow associated with both chemical and physical changes.[42] The DSC results are presented in Fig. 1d, unveiling exothermic events at 300 and 325 °C corresponding to the decomposition of PVP of molecular weight 55 000 mol g^{-1} and 136 000 mol g^{-1}, respectively. Further DSC analysis revealed an additional exothermic peak at 450 °C owing to the release of energy from carbon burning.[39] The second exothermic response is more prominent in fibers of PVP of M_w = 55 000 mol g^{-1}, which signifies a higher degree of energy liberation through carbon combustion in this sample. Thus, the rutile phase formation in the lower molecular weight PVP (M_w = 55 000 mol g^{-1}) sample at 500 °C can be ascribed to the extra energy released from carbon burning.[42] At this juncture, the carbon content in the fibre may be perceived as the fuel, and the TTIP assumes the role of

the oxidiser; hence, the overall process could be conceptualised as a combustion synthesis.[43,44] The fuel-to-oxidiser ratio is intrinsically connected to the phase of TiO$_2$ synthesised through the combustion process.[45] A higher fuel-to-oxidiser ratio can culminate in the rutile phase formation at lower temperatures.[45] The augmented carbon presence in the fiber of PVP of M_w = 55 000 mol g^{-1} has been corroborated by calcination at 350 °C and subsequent TGA analysis. After calcination at 350 °C, both samples have a black appearance owing to carbon residues, with the fibre of PVP of M_w = 55 000 mol g^{-1} showing a darker hue. The thermograms of the calcined samples are depicted in Fig. S2 in the ESI,† showing a higher mass reduction in PVP of M_w = 55 000 mol g^{-1}, which indicates surfeit carbon content in this sample after calcination at 350 °C. The TGA-DSC results indicate that the presence of surplus carbon in the fibres made of PVP of M_w = 55 000 mol g^{-1} aids the formation of a rutile phase at reduced temperatures, which is attributed to the energy released during carbon combustion.

The structure and surface morphology of the fibers were investigated using scanning electron microscopy (SEM). The SEM micrographs (Fig. 2a–c) confirm the one-dimensional fiber morphology of all the TiO$_2$ samples. The fiber structures were well retained even after calcination at 700 °C. TiO$_2$ fibers of smooth surfaces and micrometres of length were formed after calcination. The diameter distribution of the fibers is measured using Image J software, and the distribution curve is shown in the inset in Fig. 2a–c. The fibers exhibited average diameters of 200 ± 20 nm, 525 ± 20 nm, and 325 ± 15 nm for TiO$_2$-A, TiO$_2$-AR and TiO$_2$-R, respectively. The fiber diameter of TiO$_2$-AR is higher when compared to TiO$_2$-A; this increase is due to the increased weight percentage of the PVP polymer in the electrospinning sol. As has been reported by many investigators, a higher polymer concentration provides thicker diameter fibers through electrospinning.[46] The fiber diameter of the TiO$_2$-R is reduced to 325 ± 15 nm, which can be ascribed to the higher calcination temperature. The fibers tend to shrink more at higher temperatures as crystallinity and density increase.[47]

The microstructure of the fibers was further investigated using a high-resolution transmission electron microscope (HRTEM) and selected area electron diffraction (SAED) analyses. From HRTEM micrographs, it is evident that the fibers are formed with closely packed small TiO$_2$ nanocrystals. This type of structure is expected to provide direct pathways for electron transport and enhance charge collection when employed in DSC devices. The lattice fringes observed in HRTEM images and the spotty rings in SAED patterns attest to the high crystallinity of calcined fibers. Further analysis of the HRTEM images in Fig. 2g–i, TiO$_2$-A shows the lattice fringes of the anatase (101) planes with an interlayer distance of 0.359 nm, which is in close accordance with the XRD value of 0.352 nm. For TiO$_2$-R fibers, the lattice fringes displayed an interlayer distance of 0.328 nm, corresponding to the rutile (110) plane of TiO$_2$-R. Examinations of the TiO$_2$-AR HRTEM image showed lattice spacing of 0.365 nm and 0.328 nm of anatase (101) and rutile (110) planes, respectively, which implies that the fiber structure is formed through the connection of a mixture of anatase and rutile crystallites. The spots in SAED increased from TiO$_2$-A to TiO$_2$-AR
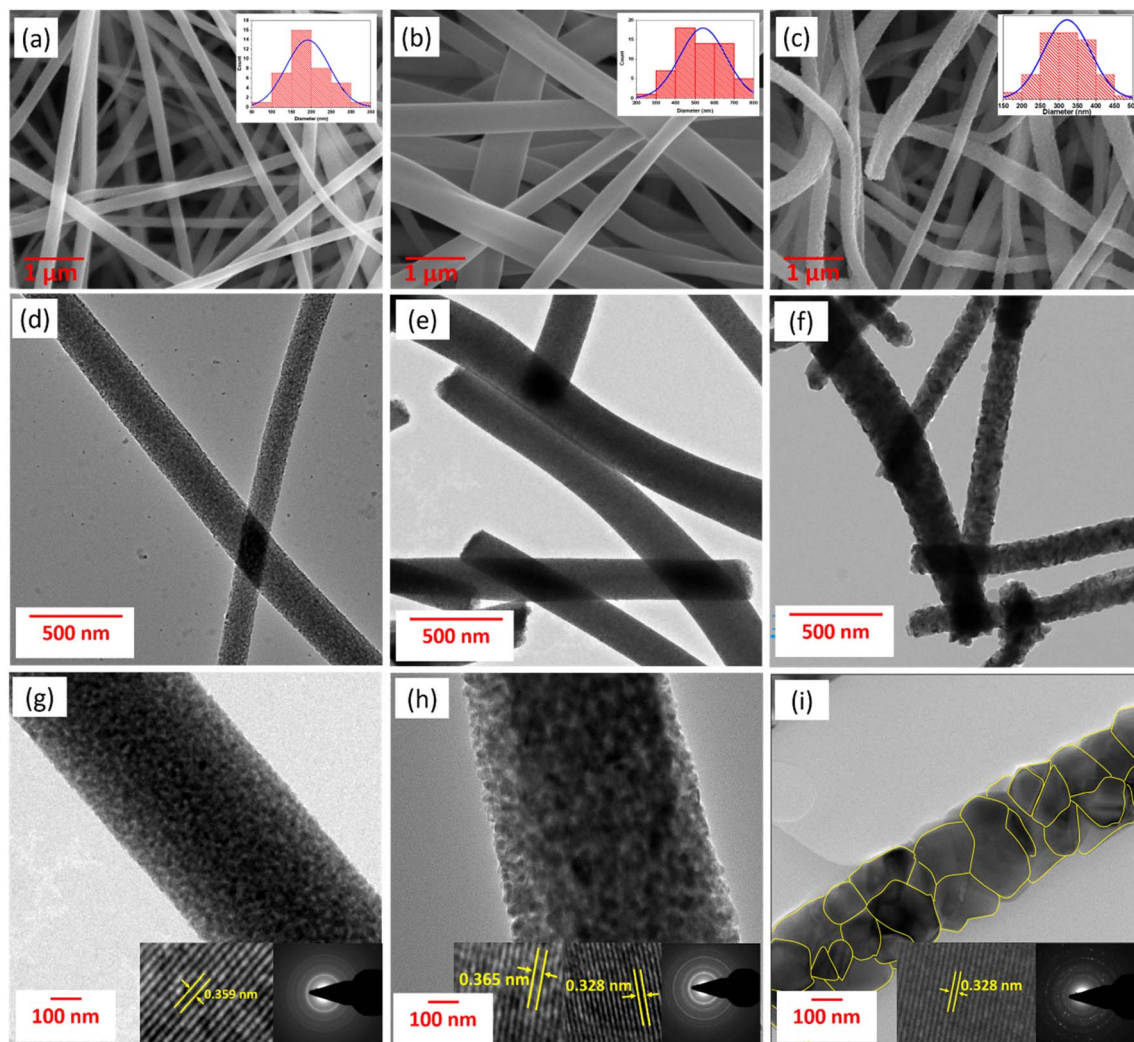
Fig. 2 SEM micrographs of (a) TiO$_2$-A, (b) TiO$_2$-AR and (c) TiO$_2$-R. (d–f) TEM images and (g–i) HRTEM images (with SAED patterns as inset) of TiO$_2$-A, TiO$_2$-AR and TiO$_2$-R, respectively.

to TiO$_2$-R, indicating an improvement in the crystallinity of the samples in the same order. The increase in crystallite size was also observed in the order TiO$_2$-A to TiO$_2$-AR to TiO$_2$-R from the HRTEM images. The crystallite size distribution of the TiO$_2$ fibers is measured using Image J software, and the distribution curves are shown in Fig. S5 in the ESI.† The crystallite size distributions well match the average crystallite sizes calculated from the XRD analysis.

The performance of the dye-sensitized solar cells fabricated using the synthesized TiO$_2$ fibers as an active layer was examined with current density–voltage (J–V) measurements under AM 1.5 G (100 mW cm^{-2}) illumination. The J–V curves are shown in Fig. 3, and the results are summarized in Table 1. The power conversion efficiency (PCE) of devices fabricated with TiO$_2$-A fiber photoanode was 3.58% ± 0.43%, with an open circuit voltage (V_{OC}) of 0.714 ± 0.006 V, short circuit current density (J_{SC}) of 7.64 ± 0.58 mA cm^{-2}, and fill factor (FF) of 65.8% ± 1.2%. Under similar conditions, the devices fabricated with TiO$_2$-R and TiO$_2$-AR exhibited much lower efficiency of 0.26% ±

0.09% and 2.17% ± 0.13%, with V_{OC} values of 0.700 ± 0.011 V and 0.706 ± 0.009 V, J_{SC} values of 0.68 ± 0.18 mA cm^{-2} and 5.08 ± 0.27 mA cm^{-2} and FF values of 54.3% ± 1.8% and 60.4% ± 1.6%, respectively. The low PCE values of TiO$_2$-R and TiO$_2$-AR devices are ascribed to their sizeable current losses. The dye desorption experiments show that the TiO$_2$-A photoanode exhibits a high dye loading of 5.14 × 10^{-8} mol cm^{-2}. In contrast, the TiO$_2$-R photoanode exhibits a low dye loading of 1.17 × 10^{-9} mol cm^{-2}, and the TiO$_2$-AR-based photoanode exhibits a moderate dye loading of 2.22 × 10^{-8} mol cm^{-2}. The amount of dye anchored onto the photoanode depends on its thickness, surface area, surface functional groups, solvents used for dye solution preparation, immersion time of photoanode in dye solution, and addition of co-adsorbents.[48] In comparison to TiO$_2$-A, both TiO$_2$-R and TiO$_2$-AR exhibit a reduced surface area owing to the tight packing of crystals and the dense nature of the fibers.

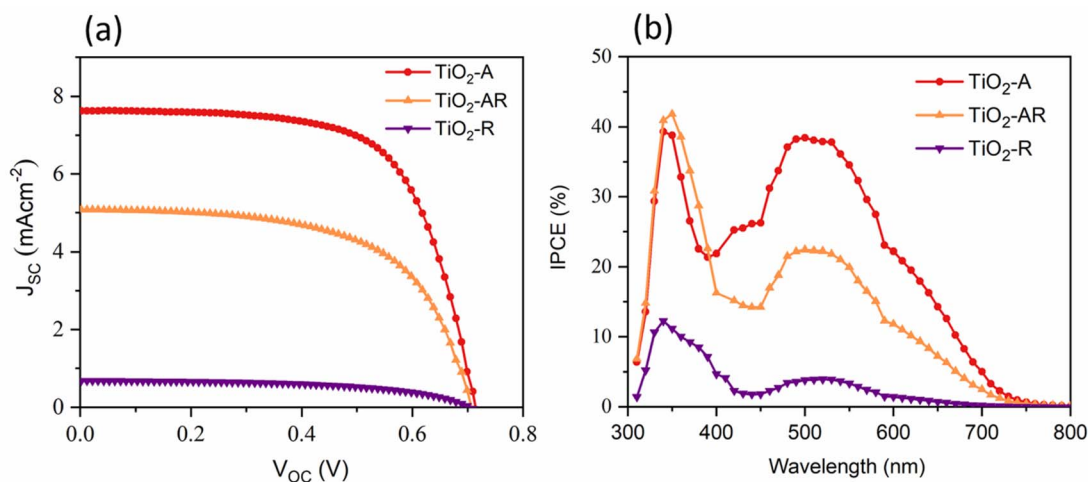Exception for the TiO$_2$ fibers, all materials and methods remain the same across the three devices. Therefore, the

Fig. 3 (a) Current density–voltage (J–V) curves under standard one sun conditions (AM 1.5 G, 100 mW cm^{-2}). (b) Incident photon to current conversion efficiency (IPCE) plot of DSCs fabricated using TiO$_2$ fibers as photoanodes.

Table 1 J–V parameters under standard one sun illumination (AM 1.5 G, 100 mW cm^{-2}), surface area and dye loading data TiO$_2$ fiber as photoanode-based DSCs

Cell	V_{OC} (V)	J_{SC} (mA cm^{-2})	FF (%)	PCE (%)	Surface area (m^2 g^{-1})	Amount of dye adsorbed (mol cm^{-2})
TiO$_2$-A	0.714 ± 0.006	7.64 ± 0.18	65.8 ± 1.2	3.58 ± 0.43	53	5.14 × 10^{-8}
TiO$_2$-R	0.700 ± 0.011	0.68 ± 0.18	54.3 ± 1.8	0.26 ± 0.09	4	1.17 × 10^{-9}
TiO$_2$-AR	0.706 ± 0.009	5.08 ± 0.27	60.4 ± 1.6	2.17 ± 0.13	40	2.22 × 10^{-8}

difference in J_{SC} can be correlated with the difference in dye loading owing to the variation in the surface area of the TiO$_2$ fibers (Table 1).

From the correlation of various data collected from characterization techniques, it is found that the current loss exhibited by TiO$_2$-R and TiO$_2$-AR devices is solely due to the decrease in dye loading in the respective devices. However, the dense nature, larger diameters and longer lengths of the fibers suggest that these structures could be ideal for use as scattering layers over nanoparticle layers. The dense nature of the fibers is expected to scatter the light more efficiently, and the direct pathways provided by the one-dimensional structure of the fibers could improve the charge collection. Therefore, we fabricated DSC photoanodes using the synthesized TiO$_2$ fibers as a scattering layer over an anatase TiO$_2$ nanoparticle (NP) active layer. The device fabricated with photoanode employing the NP active layer alone (designated as NP) exhibits an efficiency of 5.41% ± 0.3% with a V_{OC} of 0.694 ± 0.011 V, J_{SC} of 11.50 ± 0.21 mA cm^{-2} and FF of 67.7% ± 1.6%. Devices with TiO$_2$ fiber scattering layers (NP/fiber) exhibited improved performance compared to NP-based devices. The efficiency of the NP-/fiber-based device using TiO$_2$-A, TiO$_2$-R and TiO$_2$-AR scattering layers was increased by 60%, 45% and, 49%, respectively, when compared to NP-based devices. NP/fiber devices using TiO$_2$-A, TiO$_2$-R and TiO$_2$-AR scattering layers exhibited an efficiency of 8.67% ± 0.58%, 7.85% ± 0.41% and 8.06% ± 0.14%, with V_{OC} values of 0.702 ± 0.009 V, 0.706 ±

0.007 V and 0.705 ± 0.002 V, J_{SC} values of 17.71 ± 0.77 mA cm^{-2}, 16.84 ± 0.72 mA cm^{-2} and 16.78 ± 0.18 mA cm^{-2} and FF values of 69.8% ± 2.0%, 66.1% ± 0.5% and 68.2% ± 0.6%, respectively. The enhancement in performance is mainly attributed to the improvement in J_{SC}, which can be primarily ascribed to better light harvesting through improved light scattering.

Incident photon to current conversion efficiency (IPCE) spectra of the devices (Fig. 4b) provide details on the light-harvesting ability. The NP devices have a lower IPCE, which is in accordance with the J–V results. On comparing the IPCE spectra of NP device and NP/fiber devices, a 29% IPCE improvement was observed at 520 nm when the TiO$_2$-A fiber scattering layer was applied over the NP active layer, followed by 15% and 19% improvement for TiO$_2$-R and TiO$_2$-AR scattering layer-based devices, respectively. Additionally, the introduction of fiber scattering layers changes the behaviour of the IPCE spectra at higher wavelengths. An extra shoulder peak emerges at 590 nm, and the IPCE onset extends to around 750 nm. This improvement in IPCE and the shift of IPCE onset to the longer wavelength can be explained by the significant light scattering ability of TiO$_2$ fibers.[49] Such scattering is expected to trap more light within the device, leading to increased light harvesting as observed in our case (Table 2).

The reflectance and transmittance of photoanodes are evaluated using a UV-Vis-NIR spectrometer equipped with an integrating sphere. As shown in Fig. 4c, the NP photoanode exhibits a very low reflectance, and more than 40% of the incident light
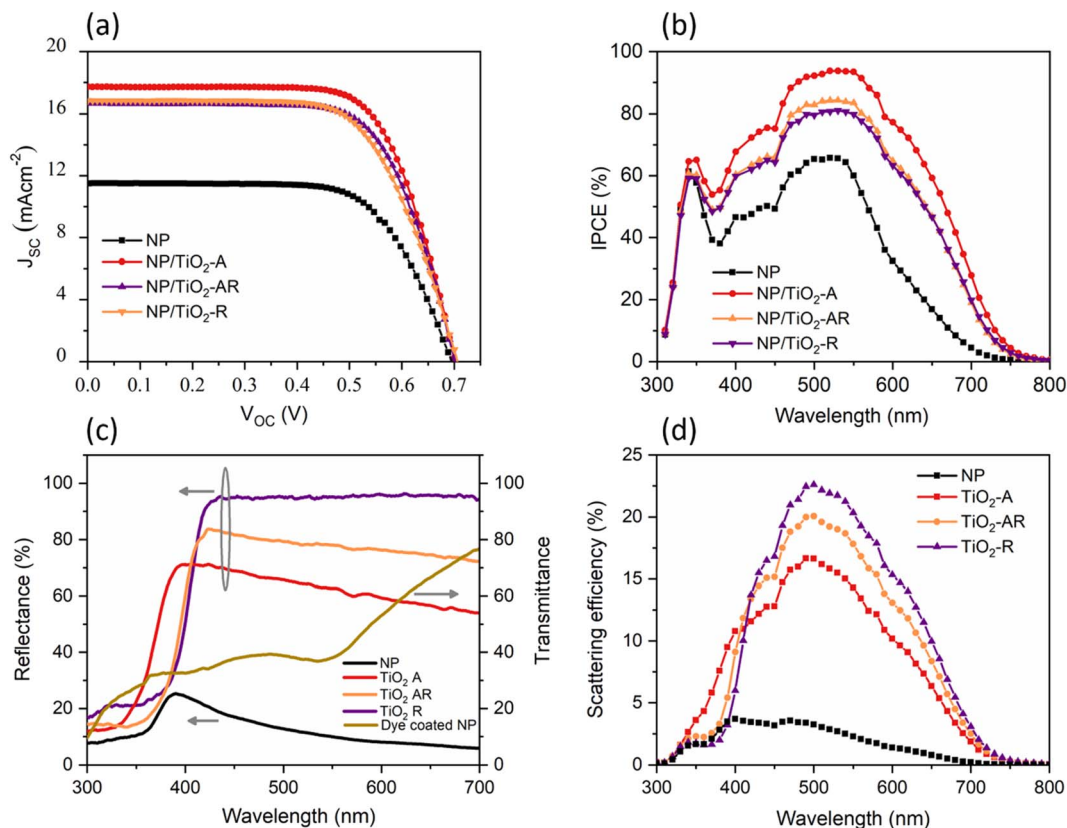
Fig. 4 (a) *J–V* curves under standard one sun illumination (AM 1.5 G, 100 mW cm^{-2}), (b) IPCE plot of DSCs fabricated using TiO$_2$ fibers as scattering layer, (c) reflectance and transmittance spectra of TiO$_2$ nanoparticles and fiber films, and (d) scattering efficiency of TiO$_2$ fiber scattering layer.

is transmitted through the dye-coated NP photoanodes without being absorbed. The transmittance gradually increases after 550 nm, and it reaches up to 77% at 700 nm. In contrast, the TiO$_2$ fibers, with high crystallinity and dense nature, exhibit very high reflectance in the visible region. The order of reflectance increased from TiO$_2$-A to TiO$_2$-AR to TiO$_2$-R; the increase in reflectance follows the amount of rutile phase present in the sample; this implies that the higher refractive index of the rutile phase helps to scatter the light more effectively.[50] It is also imperative to consider that the TiO$_2$-R samples exhibit well-defined large grains, as confirmed by the TEM analysis, which effectively reflects the incident light. When applied to the NP layer, the TiO$_2$ fibers enhance the light absorption of the dye-coated NP/fiber double-layer photoanode by backscattering the light transmitted through the NP layer. The backscattering increases the path length and prolongs the duration of light

inside the photoanode, leading to increased light absorption. The higher J_{SC} observed in the TiO$_2$ fiber scattering layer-based devices than in the NP photoanode devices is a direct result of this increased light absorption. The scattering efficiency of the TiO$_2$ fiber layers is computed using eqn (3):

$$\text{Scattering efficiency} = T_{NP}R_F\text{IPCE}_{NP} \qquad (3)$$

where T_{NP} represents the transmittance of the dye-coated NP photoanode film, R_F is the reflectance of the TiO$_2$ fiber layer alone, and IPCE$_{NP}$ denotes the IPCE of the NP photoanode device.[51] Fig. 4d depicts the calculated scattering efficiency of the TiO$_2$ fiber layers over the NP layer as a function of wavelength. The graph follows a shape previously reported by Koo *et al.* in their size-dependent scattering study.[51] Compared to their results, our study exhibits a broad shape for the scattering efficiency, which is in the range of 400–700 nm, with high scattering efficiency percentages. This broad shape and high scattering efficiency can be attributed to the effective scattering of transmitted light by TiO$_2$ fibers over a wide range owing to their high crystallinity and dense one-dimensional structure. The maximum scattering efficiency observed around the 500 nm wavelength is due to the maximum absorbance of the N719 dye in that wavelength range.

As shown in Fig. 4d, the TiO$_2$-R layer exhibits higher scattering efficiency than the TiO$_2$-A and TiO$_2$-AR layers, which can

Table 2 *J–V* parameters under standard one sun illumination (AM 1.5 G, 100 mW cm^{-2}), *J–V* parameters of DSCs

Cell	V_{OC} (V)	J_{SC} (mA cm^{-2})	FF	Efficiency (%)
NP	0.694 ± 0.011	11.50 ± 0.21	67.8 ± 1.6	5.41 ± 0.31
NP/TiO$_2$-A	0.702 ± 0.009	17.71 ± 0.77	69.8 ± 2.0	8.67 ± 0.58
NP/TiO$_2$-R	0.706 ± 0.007	16.84 ± 0.72	66.1 ± 0.5	7.85 ± 0.47
NP/TiO$_2$-AR	0.705 ± 0.002	16.78 ± 0.18	68.2 ± 0.6	8.06 ± 0.14

be attributed to the higher reflectance of the material. Interestingly, it is observed that the highest PCE is achieved for the TiO$_2$-A layer, which has a lower scattering efficiency. These findings suggest that the performance improvement of NP/fiber devices is not solely influenced by light scattering but also by other factors. The device performance parameters indicate that the efficiency of NP/fiber devices is improved by the enhancement in J_{SC}. Dye loading is another critical factor that directly affects the J_{SC}. As explained in the previous discussion, the dye loading is significantly reduced from TiO$_2$-A to TiO$_2$-AR to TiO$_2$-R. Therefore, it is inferred that in NP/TiO$_2$-A devices, the dye molecules anchored onto the TiO$_2$-A scattering layer absorb the incident light and contribute to the J_{SC} improvement in addition to its light scattering. It must be noted that even though the scattering efficiency of TiO$_2$-A is lower than that of TiO$_2$-R and TiO$_2$-AR, it is much higher than the scattering efficiency of NPs. Hence, the combined effect of light scattering and dye loading of the TiO$_2$-A fibers contributed to the enhanced overall PCE of NP/TiO$_2$-A-based bilayer devices. However, in the case of the NP/TiO$_2$-R, the improvement in J_{SC} is solely ascribed to the higher scattering efficiency of the TiO$_2$-R layer, as its dye loading is very low. As the TiO$_2$-AR has scattering efficiency and dye loading between TiO$_2$-A and TiO$_2$-R, the PCE of NP/TiO$_2$-AR lies between the two. The results indicate that a material with high scattering

efficiency and good dye loading properties can act as an ideal scattering material for bilayer DSCs to deliver a higher PCE by enhancing light harvesting and improving J_{SC}. The application of the scattering layer helps to increase the light harvesting ability of the photoanode. However, it increases film thickness, which may affect charge collection.

To gain insight into the impact of the TiO$_2$ fiber scattering layer over the active layer on the charge transfer dynamics in DSCs, we carried out electrochemical impedance spectroscopy (EIS), transient photovoltage decay, and transient photocurrent decay measurements. The Nyquist plot at a bias potential equivalent to the V_{OC} of the devices, along with the equivalent circuit used to fit the EIS data, is illustrated in Fig. 5a. The electron lifetime obtained by fitting the EIS (Nyquist) (Fig. 5b) revealed that the NP/TiO$_2$-A photoanodes with a one-dimensional structure and reduced grain boundaries exhibit a higher electron lifetime than the NP photoanodes. The results are further supported by the dark current and transient photovoltage decay measurements, as illustrated in Fig. S7.† The transport time measurements (Fig. 5c and S8†) reveal that despite a 50% increase in film thickness, the change in transport time is minimal for NP/TiO$_2$-A photoanode owing to the faster electron transport through the one-dimensional TiO$_2$-A fibers. Charge collection efficiency (η_{cc}) quantifies the
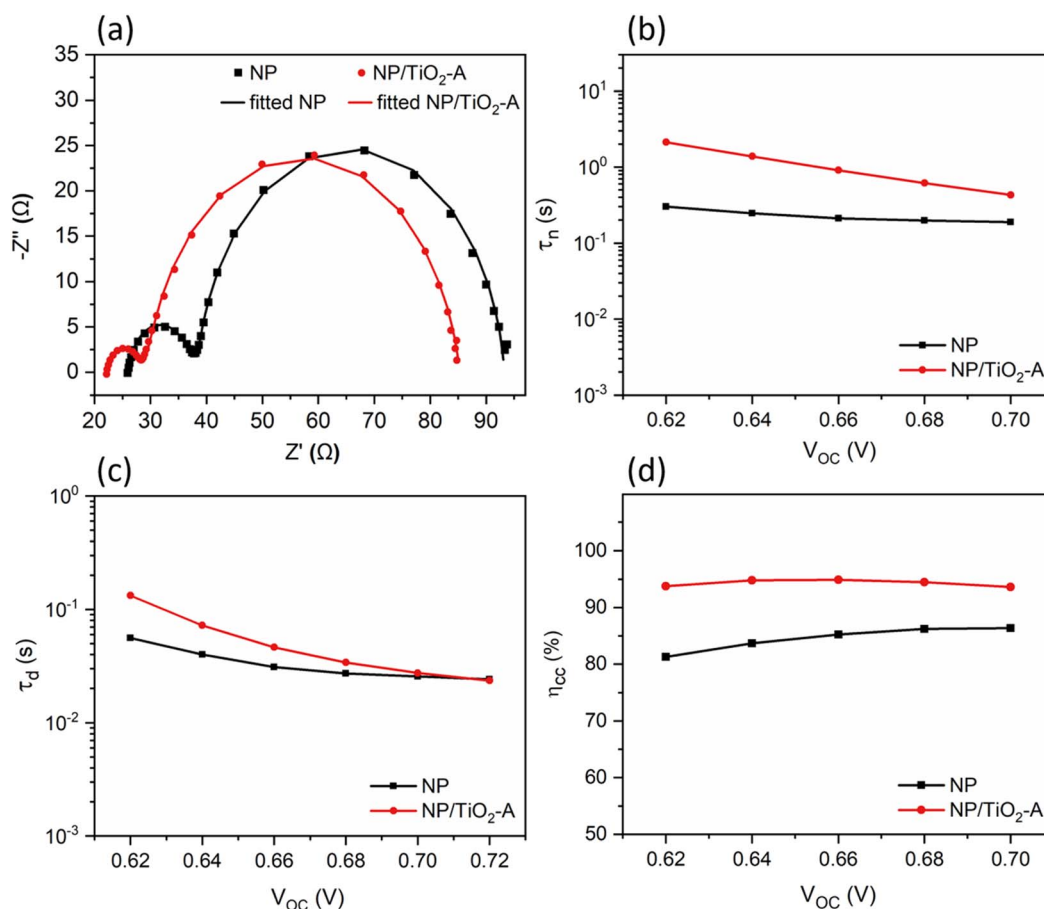

Fig. 5 (a) Nyquist plot with equivalent circuit, (b) electron lifetime, (c) transport time and (d) charge collection efficiency as a function of open circuit voltage of NP and NP/TiO$_2$-A DSCs.

effectiveness of collecting injected electrons at the back contact. For efficient charge collection, DSC photoanodes must exhibit a longer electron lifetime and rapid electron diffusion within their mesoporous structures. Fig. 5d shows that the NP/TiO$_2$-A devices exhibit better η_{cc} compared to NP photoanode devices, attributed to their improved electron lifetime and comparable transport time. This improved η_{cc} significantly contributes to the superior short-circuit current density (J_{SC}) and, consequently, to the higher power conversion efficiency (PCE) of NP/TiO$_2$-A devices.

IV. Conclusion

TiO$_2$ fibers of different phases were synthesized using the electrospinning technique by carefully modifying the sol composition and calcination temperatures. The influence of polyvinylpyrrolidone (PVP) molecular weight and concentration on TiO$_2$ crystallization was systematically investigated through TGA-DSC analysis. The results demonstrate that anatase or mixed anatase–rutile phase TiO$_2$ fibers can be obtained by adjusting the molecular weight and weight percentage of PVP in the sol. The formation of the rutile phase in fibers with a higher polymer content at lower calcination temperatures is attributed to the additional energy released during the combustion of surplus carbon formed upon decomposition. The synthesised TiO$_2$ fibers are applied in DSC photoanode as a scattering layer on top of a nanoparticle TiO$_2$ layer. The PCE of nanoparticle-based devices increased by 60%, 49% and 45% when TiO$_2$-A, TiO$_2$-AR and TiO$_2$-R fibers were applied as scattering layers, respectively. The IPCE and scattering efficiency calculation results indicated that the dense crystalline TiO$_2$-R fiber scattering layers effectively scatter light, thus improving the light harvesting of NP/TiO$_2$-R devices and achieving a higher PCE. The TiO$_2$-A scattering layer contributed to light scattering and exhibited higher dye loading, further enhancing the short-circuit current density (J_{SC}) and resulting in the highest PCE (8.67%) for NP/TiO$_2$-A-based bilayer devices. The NP/TiO$_2$-AR device, with scattering efficiency and dye loading intermediates between those of TiO$_2$-A and TiO$_2$-R, achieved a corresponding PCE that fell between the two. Interfacial charge transfer studies revealed that the NP/fiber bilayer structure provided an optimal balance between electron lifetime and transport time, reducing charge recombination and enhancing charge collection efficiency, which collectively improved device performance. In conclusion, this study demonstrates the synthesis of TiO$_2$ fibers with tunable phases using the electrospinning technique and highlights their potential as scattering layers in DSC photoanodes. One-dimensional TiO$_2$ nanofibers with high scattering efficiency, improved dye loading, and enhanced charge collection properties represent an ideal scattering material for DSCs, significantly boosting light harvesting and reducing recombination to achieve superior PCE.

Data availability

This research work was carried out in our laboratory, and the primary data are produced by us using various equipments available in our laboratory. No public data are used in this study. Some of the data supporting this study are included in the ESI.†

Author contributions

PSD and SS conceived the idea and coordinated the work. MM synthesized the materials and carried out all characterizations. MM and AJ fabricated the solar cells and conducted measurements and data analyses. KNU contributed to the manuscript corrections and preparations. MM wrote the manuscript, and other co-authors revised it. All authors commented on the manuscript.

Conflicts of interest

There are no conflicts to declare.

Acknowledgements

References

1 D. K. Kumar, J. Kříž, N. Bennett, B. Chen, H. Upadhayaya, K. R. Reddy and V. Sadhu, Functionalized metal oxide nanoparticles for efficient dye-sensitized solar cells (DSSCs): a review, *Mater. Sci. Energy Technol.*, 2020, **3**, 472–481.

2 Y. Ren, D. Zhang, J. Suo, Y. Cao, F. T. Eickemeyer, N. Vlachopoulos, S. M. Zakeeruddin, A. Hagfeldt and M. Grätzel, Hydroxamic acid pre-adsorption raises the efficiency of cosensitized solar cells, *Nature*, 2023, **613**, 60–65.

3 P. R. Jebin, A. S. George, R. K. Mishra, J. John and S. Soman, Enhanced indoor photovoltaic efficiency of 40% in dye-sensitized solar cells using cocktail starburst triphenylamine dyes and dual-species copper electrolyte, *J. Mater. Chem. A*, 2024, 32721–32734.

4 A. S. George, S. C. Pradhan, K. N. N. Unni and S. Soman, Engineered hole-free, spacer-free dye-sensitized light harvesters for indoor photovoltaic and self-powered applications, *RSC Sustainability*, 2024, **2**, 2839–2843.

5 M. N. Rajesh, A. S. George, S. M. Meethal, S. Dasgupta, S. Soman and L. Giribabu, Maximizing Indoor Light-Harvesting Efficiency Using Molecularly Engineered Triphenylimidazole-Phenothiazine Dyes and Dual-Species Copper Electrolyte, *ACS Appl. Energy Mater.*, 2024, **7**, 7864–7874.

6 S. M. Meethal, S. C. Pradhan, J. Velore, S. Varughese, R. S. Pillai, F. Sauvage, A. Hagfeldt and S. Soman, Asymmetric dual species copper(ii/i) electrolyte dye-sensitized solar cells with 35.6% efficiency under indoor light, *J. Mater. Chem. A*, 2024, **12**, 1081–1093.

7 A. Hagfeldt, G. Boschloo, L. Sun, L. Kloo and H. Pettersson, Dye-sensitized solar cells, *Chem. Rev.*, 2010, **110**, 6595–6663.

8 S. C. Pradhan, A. Hagfeldt and S. Soman, Resurgence of DSCs with copper electrolyte: a detailed investigation of interfacial charge dynamics with cobalt and iodine based electrolytes, *J. Mater. Chem. A*, 2018, **6**, 22204–22214.

9 J. Velore, S. C. Pradhan, T. W. Hamann, A. Hagfeldt, K. N. N. Unni and S. Soman, Understanding Mass Transport in Copper Electrolyte-Based Dye-Sensitized Solar Cells, *ACS Appl. Energy Mater.*, 2022, **5**, 2647–2654.

10 L. Sivasankaran, S. C. Pradhan, R. K. Mishra, S. Soman and A. Ajayaghosh, Role of alkyl groups regulating recombination and mass transport at cobalt electrolyte-dye interface in dye sensitized solar cells, *Sol. Energy*, 2022, **236**, 182–194.

11 S. C. Pradhan, J. Velore, S. M. Meethal and S. Soman, Fundamental Understanding of Dye Coverage and Performance in Dye-Sensitized Solar Cells Using Copper Electrolyte, *Energies*, 2023, **16**, 6913.

12 M. N. Mustafa and Y. Sulaiman, Review on the effect of compact layers and light scattering layers on the enhancement of dye-sensitized solar cells, *Sol. Energy*, 2021, **215**, 26–43.

13 A. Jagadeesh, G. Veerappan, P. S. Devi, K. N. N. Unni and S. Soman, Synergetic effect of TiO₂/ZnO bilayer photoanodes realizing exceptionally high VOC for dye-sensitized solar cells under outdoor and indoor illumination, *J. Mater. Chem. A*, 2023, **11**, 14748–14759.

14 S. Sasidharan, S. C. Pradhan, A. Jagadeesh, B. N. Nair, A. A. P. Mohamed, K. N. N. Unni, S. Soman and U. N. S. Hareesh, Bifacial Dye-Sensitized Solar Cells with Enhanced Light Scattering and Improved Power Conversion Efficiency under Full Sun and Indoor Light Conditions, *ACS Appl. Energy Mater.*, 2020, **3**, 12584–12595.

15 S. Sasidharan, A. Jagadeesh, S. C. Pradhan, B. N. Nair, A. A. P. Mohamed, K. N. N. Unni, S. Soman and U. N. S. Hareesh, ZnO hierarchical structures as sacrificial inclusions for enhanced performance under full sun and indoor light in bifacial dye sensitized solar cells, *Sol. Energy*, 2021, **226**, 214–224.

16 I. Concina and A. Vomiero, Metal oxide semiconductors for dye- and quantum-dot-sensitized solar cells, *Small*, 2015, **11**, 1744–1774.

17 J.-Y. Liao, J.-W. He, H. Xu, D.-B. Kuang and C.-Y. Su, Effect of TiO₂ morphology on photovoltaic performance of dye-sensitized solar cells: nanoparticles, nanofibers, hierarchical spheres and ellipsoid spheres, *J. Mater. Chem.*, 2012, **22**, 7910–7918.

18 F. Zhu, D. Wu, Q. Li, H. Dong, J. Li, K. Jiang and D. Xu, Hierarchical TiO₂ microspheres: synthesis, structural control and their applications in dye-sensitized solar cells, *RSC Adv.*, 2012, **2**, 11629–11637.

19 S. C. Pradhan, J. Velore, A. Hagfeldt and S. Soman, Probing photovoltaic performance in copper electrolyte dye-sensitized solar cells of variable TiO₂ particle size using comprehensive interfacial analysis, *J. Mater. Chem. C*, 2022, **10**, 3929–3936.

20 P. Joshi, L. Zhang, D. Davoux, Z. Zhu, D. Galipeau, H. Fong and Q. Qiao, Composite of TiO₂ nanofibers and nanoparticles for dye-sensitized solar cells with significantly improved efficiency, *Energy Environ. Sci.*, 2010, **3**, 1507–1510.

21 X. Wang, G. He, H. Fong and Z. Zhu, Electron Transport and Recombination in Photoanode of Electrospun TiO₂ Nanotubes for Dye-Sensitized Solar Cells, *J. Phys. Chem. C*, 2013, **117**, 1641–1646.

22 J. Xue, T. Wu, Y. Dai and Y. Xia, Electrospinning and Electrospun Nanofibers: Methods, Materials, and Applications, *Chem. Rev.*, 2019, **119**, 5298–5415.

23 J. G. López-Covarrubias, L. Soto-Muñoz, A. L. Iglesias and L. J. Villarreal-Gómez, Electrospun Nanofibers Applied to Dye Solar Sensitive Cells: A Review, *Materials*, 2019, **12**, 3190.

24 T. Wan, S. Ramakrishna and Y. Liu, Recent progress in electrospinning TiO₂ nanostructured photo-anode of dye-sensitized solar cells, *J. Appl. Polym. Sci.*, 2018, **135**, 45649.

25 X. Wang, S. Karanjit, L. Zhang, H. Fong, Q. Qiao and Z. Zhu, Transient photocurrent and photovoltage studies on charge transport in dye sensitized solar cells made from the composites of TiO₂ nanofibers and nanoparticles, *Appl. Phys. Lett.*, 2011, **98**, 82114.

26 P. F. Du, L. X. Song and J. Xiong, Enhanced conversion efficiency in dye-sensitized solar cells based on bilayered nano-composite photoanode film consisting of TiO₂ nanoparticles and nanofibers, *J. Nanosci. Nanotechnol.*, 2014, **14**, 4164–4169.

27 G. Wang, W. Xiao and J. Yu, High-efficiency dye-sensitized solar cells based on electrospun TiO₂ multi-layered composite film photoanodes, *Energy*, 2015, **86**, 196–203.

28 A. Roy, S. Mukhopadhyay, P. S. Devi and S. Sundaram, Polyaniline-Layered Rutile TiO₂ Nanorods as Alternative Photoanode in Dye-Sensitized Solar Cells, *ACS Omega*, 2019, **4**, 1130–1138.

29 S. Kailasa, M. S. B. Reddy, M. R. Maurya, B. G. Rani, K. V. Rao and K. K. Sadasivuni, Electrospun Nanofibers: Materials, Synthesis Parameters, and Their Role in Sensing Applications, *Macromol. Mater. Eng.*, 2021, **306**, 2100410.

30 S. Chattopadhyay, J. Saha and G. De, Electrospun anatase TiO₂ nanofibers with ordered mesoporosity, *J. Mater. Chem. A*, 2014, **2**, 19029–19035.

31 S. Ito, P. Chen, P. Comte, M. K. Nazeeruddin, P. Liska, P. Péchy and M. Grätzel, Fabrication of screen-printing pastes from TiO₂ powders for dye-sensitised solar cells, *Prog. Photovoltaics*, 2007, **15**, 603–612.

32 E. Dell'Orto, L. Raimondo, A. Sassella and A. Abbotto, Dye-sensitized solar cells: spectroscopic evaluation of dye loading on TiO₂, *J. Mater. Chem.*, 2012, **22**, 11364–11369.

33 S. C. Pradhan, J. Velore, A. Hagfeldt and S. Soman, Probing photovoltaic performance in copper electrolyte dye-

sensitized solar cells of variable TiO$_2$ particle size using comprehensive interfacial analysis, *J. Mater. Chem. C*, 2022, **10**, 3929–3936.

34 M. Lal, P. Sharma and C. Ram, Calcination temperature effect on titanium oxide (TiO$_2$) nanoparticles synthesis, *Optik*, 2021, **241**, 166934.

35 K. Wang, Y. Zhuo, J. Chen, D. Gao, Y. Ren, C. Wang and Z. Qi, Crystalline phase regulation of anatase–rutile TiO$_2$ for the enhancement of photocatalytic activity, *RSC Adv.*, 2020, **10**, 43592–43598.

36 S. Challagulla, K. Tarafder, R. Ganesan and S. Roy, Structure sensitive photocatalytic reduction of nitroarenes over TiO$_2$, *Sci. Rep.*, 2017, **7**, 8783.

37 Utkarsh, H. Hegab, M. Tariq, N. A. Syed, G. Rizvi and R. Pop-Iliev, Towards Analysis and Optimization of Electrospun PVP (Polyvinylpyrrolidone) Nanofibers, *Adv. Polym. Technol.*, 2020, **2020**, 4090747.

38 O. Secundino-Sánchez, J. Diaz-Reyes, J. Aguila-López and J. F. Sánchez-Ramírez, Crystalline phase transformation of electrospinning TiO$_2$ nanofibres carried out by high temperature annealing, *J. Mol. Struct.*, 2019, **1194**, 163–170.

39 J. Zhang, Y. Cai, X. Hou, H. Zhou, H. Qiao and Q. Wei, Preparation of TiO$_2$ Nanofibrous Membranes with Hierarchical Porosity for Efficient Photocatalytic Degradation, *J. Phys. Chem. C*, 2018, **122**, 8946–8953.

40 A. Mamun, S. M. M. Rahman, S. Roland and R. Mahmood, Impact of Molecular Weight on the Thermal Stability and the Miscibility of Poly(ε-caprolactone)/Polystyrene Binary Blends, *J. Polym. Environ.*, 2018, **26**, 3511–3519.

41 B. D. Fahlman, *Materials Chemistry*, Springer Netherlands, 2011, pp. 31–189.

42 J. D. Menczel, L. Judovits, R. B. Prime, H. E. Bair, M. Reading and S. Swier, in *Thermal Analysis of Polymers*, 2009, pp. 7–239.

43 R. D. Purohit, B. P. Sharma, K. T. Pillai and A. K. Tyagi, Ultrafine ceria powders via glycine-nitrate combustion, *Mater. Res. Bull.*, 2001, **36**, 2711–2721.

44 J. C. Toniolo, M. D. Lima, A. S. Takimi and C. P. Bergmann, Synthesis of alumina powders by the glycine–nitrate combustion process, *Mater. Res. Bull.*, 2005, **40**, 561–571.

45 S. Challagulla and S. Roy, The role of fuel to oxidizer ratio in solution combustion synthesis of TiO$_2$ and its influence on photocatalysis, *J. Mater. Res.*, 2017, **32**, 2764–2772.

46 S. Santibenchakul, S. Chaiyasith and W. Pecharapa, Effect of PVP concentration on microstructure and physical properties of electrospun SnO$_2$ nanofibers, *Integr. Ferroelectr.*, 2016, **175**, 130–137.

47 S. S. Mali, C. S. Shim, H. Kim, J. V. Patil, D. H. Ahn, P. S. Patil and C. K. Hong, Evaluation of various diameters of titanium oxide nanofibers for efficient dye sensitized solar cells synthesized by electrospinning technique: a systematic study and their application, *Electrochim. Acta*, 2015, **166**, 356–366.

48 P. Gnida, M. Libera, A. Pająk and E. Schab-Balcerzak, Examination of the Effect of Selected Factors on the Photovoltaic Response of Dye-Sensitized Solar Cells, *Energy Fuels*, 2020, **34**, 14344–14355.

49 H. Wang, B. Wang, J. Yu, Y. Hu, C. Xia, J. Zhang and R. Liu, Significant enhancement of power conversion efficiency for dye sensitized solar cell using 1D/3D network nanostructures as photoanodes, *Sci. Rep.*, 2015, **5**, 9305.

50 E. S. Thiele and R. H. French, Light-Scattering Properties of Representative, Morphological Rutile Titania Particles Studied Using a Finite-Element Method, *J. Am. Ceram. Soc.*, 1998, **81**, 469–479.

51 H.-J. Koo, J. Park, B. Yoo, K. Yoo, K. Kim and N.-G. Park, Size-dependent scattering efficiency in dye-sensitized solar cell, *Inorg. Chim. Acta*, 2008, **361**, 677–683.